Single-cell transcriptome sequencing for opening the blood-brain barrier through specific mode electroacupuncture stimulation

Congcong Ma[1,2,3†], Zhaoxing Jia[2†], Tianxiang Jiang[2†], Qian Cai[2†], Jinding Yang[2†], Lin Gan[2], Kecheng Qian[2], Zixin Pan[2], Qinyu Ye[2], Mengyuan Dai[4], Xianming Lin[1,2,3]*

[1]Third Affiliated Hospital of Zhejiang Chinese Medical University, Moganshan Road No. 219, Xihu District, Zhejiang Province 310012, China

[2]The Third Clinical Medical College, Zhejiang Chinese Medical University, No. 548 Binwen Road, Binjiang District, Hangzhou 310053, China

[3]Key Laboratory of Acupuncture and Neurology of Zhejiang Province, No. 548 Binwen Road, Binjiang District, Hangzhou 310053, China

[4]Department of Rehabilitation, Lishui Central Hospital, No. 289, Kuocang Road, Liandu District, LiShui 323000, China

[†]These authors contributed equally to this work and should be considered co-first authors.

*__Correspondence to__: Xianming Lin

The Third Affiliated Hospital of Zhejiang Chinese Medical University

Moganshan Road No. 219, Xihu District, Zhejiang Province 310005, China

Phone: 13858028101

Fax: 0571-88393511

Email: linxianming1966@163.com

ORCID: 0000-0002-2729-8324

Abstract

Background: The blood-brain barrier (BBB) interferes with the treatment of central nervous system disorders owing to the complexity of its structure and restrictive function. Thus, it is challenging to develop central nervous system drug delivery strategies. Specific mode electroacupuncture (EA) stimulation can effectively open the BBB in rats.

Methods: Here, we used single-cell RNA sequencing (scRNA-seq) to comprehensively map the cell population in the rat cerebral cortex.

Results: We identified 23 cell subsets and eight types of cells in the brain by cell annotation. scRNA-seq revealed transcriptional changes in the cerebral cortex under EA.

Conclusions: Our findings offer valuable insights into the molecular and cellular modifications in the brain resulting from EA intervention and serve as a resource for drug delivery across healthy and diseased states. Innovative approaches to enhance BBB opening will lead to more effective therapeutic plans and enhanced drug delivery.

Funding: This work was supported by the National Natural Science Foundation of China [Xianming Lin: grant numbers 82174502, 82474626]; Zhejiang provincial natural science foundation [Congcong Ma: grant number LQN25H270008]; Special Project of Modernization of Traditional Chinese Medicine in Zhejiang Province in 2022 [Xianming Lin: grant number 2022ZX009]; Scientific Research Project of the Affiliated Hospital of Zhejiang Chinese Medical University in 2022 [Xianming Lin: grant number 2022FSYYZZ10]; Scientific Research Project of the Affiliated Hospital of Zhejiang Chinese Medical University in 2023 [Congcong Ma: grant number 2023FSYYZQ11]. The funders had no role in the study design, data collection and interpretation, or the decision to submit the work for publication.

Keywords: blood-brain barrier; central nervous system; drug delivery; single-cell RNA sequencing; bioinformatics analysis; transcriptional change

Introduction

The blood-brain barrier (BBB), which is crucial for drug delivery to the brain, mainly comprises specialized brain endothelial cells with tight junctions, a basement membrane, neurons, pericytes, and astrocytes. Its chemical composition and physical properties create an adaptable interface. Single-cell RNA sequencing (scRNA-seq) can systematically identify cell types and post-intervention molecular changes by analyzing the gene expression profiles of individual cells. This enables researchers to infer cell type-specific interactions and predict the molecular basis and functional significance of these ligand-receptor interactions.

Our previous research revealed that electroacupuncture (EA) employing the parameters of “2/100 Hz, 3 mA, 6 s-6 s, 40 min” at the head stimulation points (Baihui and Shuigou acupoints) yields a notably effective BBB opening effect. Nevertheless, the mechanism remains largely unknown (Zhang et al., 2018; Zhang et al., 2020; Ma et al., 2022; Lin et al., 2023; Ma et al., 2024; Dai et al., 2025). Here, we addressed this challenge by presenting a comprehensive single-cell molecular map of the rat frontal cortex, which covers approximately 98,338 cells from 10 samples, including freshly excised cortical brain tissue after EA intervention and responsive tissue from the control group. We characterized 23 clusters in the rat frontal cortex, including eight annotated cell types.

Methods

Animal model

Male Sprague–Dawley rats (Specific Pathogen Free), 8–10 weeks old and weighing 180–220 g, were obtained from Shanghai Sipul-Bike Experimental Animal Company. All mice were

housed in the Zhejiang Chinese Medical University Laboratory Animal Research Center under a 12-h light/dark cycle with food and water given ad libitum. Rats were group-housed and were randomly assigned to experimental groups.

Materials and methods

Grouping and interventions

Rats were randomly assigned to the EA and CON groups (n = 5 per group). The EA group received EA; the CON group received the same non-stimulated binding treatment. Sterile disposable needles from Beijing Zhongyan Taihe Medical Equipment Co., Ltd. (Beijing, China) were used for EA. The GV20 (Baihui) and GV26 (Shuigou) acupuncture points were selected, with needle dimensions of 25 mm x 0.13 mm for GV20 and 16 mm × 0.07 mm for GV26. A custom relay, connected to an acupuncture point stimulator (HANS-200A, Nanjing Jisheng Co., Ltd., Nanjing, China), activated the needles in a 6 s on/off cycle. The current was set at 3 mA at a frequency of 2/100 Hz, and the stimulation lasted for 40 min.

Cerebral cortex issue preparation

At the conclusion of the experiments, rats were anesthetized using intraperitoneally administered pentobarbital (50 mg/kg). Subsequently, normal saline solution was circulated through the left side of the heart. The brain was removed via decapitation, and the frontal cortex tissue was immediately separated and placed in an ice-cold sterile RNase-free culture dish with an appropriate amount of calcium-free and magnesium-free 1 × phosphate-buffered saline (PBS). The tissue was then sliced into 0.5-mm^3 pieces and washed with 1 × PBS. Non-target tissues, such as the blood cells and brain white matter, were carefully removed.

Single cells were isolated using a previously described method (Chi et al., 2024). Standard cDNA amplification and library construction were performed. The libraries were

sequenced on an Illumina NovaSeq 6000 system (paired-end, 150 bp) by LC-BioTechnology Co., Ltd. (Hangzhou, China) with a minimum depth of 20,000 reads per cell.

Quantification and statistical analysis

Bioinformatics analysis

Sequencing results were demultiplexed and converted to the FASTQ format using Illumina bcl2fastq (version 2.20). The Cell Ranger pipeline (v6.1.1; <https://support.10xgenomics.com/single-cell-gene-expression/software/pipelines/latest/what-is-cell-ranger>) handles sample demultiplexing, barcode processing, and single-cell 3' gene counting. From five EA and five CON samples, 98,338 single cells were captured using the 10X Genomics Chromium Single Cell 3' solution. The output was analyzed using Seurat (version 3.1.1) for dimensional reduction, clustering, and scRNA-seq data analysis. Quality control filtered cells with fewer than 500 expressed genes, UMI counts below 500, and >25% mitochondrial DNA-derived gene expression; as a result, 80,713 cells were included in the analysis.

To enhance data visualization, we used Seurat for the dimensionality reduction of all cells, followed by t-distributed stochastic neighbor embedding (t-SNE) for two-dimensional projection. The process included 1) applying the LogNormalize method from Seurat's “Normalization” function to determine the gene expression values; 2) conducting principal component analysis (PCA) of normalized expression values, selecting the top 10 principal components (PCs) for clustering and t-SNE analysis; 3) using the weighted shared nearest neighbor (SNN) graph-based clustering method to identify clusters; and 4) selecting marker genes for each cluster using the Wilcoxon rank-sum test (default parameters “bimod” and the likelihood ratio test) via Seurat's FindAllMarkers function. Marker genes were chosen based

on their expression in more than 10% of cells within a cluster, with an average log value (fold change) greater than 0.25 (default parameter: 0.26).

Bioinformatics analysis was performed using the OmicStudio tools, which are accessible at https://www.omicstudio.cn/tool.

Doublet removal

Occasionally, two or more cells are encapsulated in the same gem during single-cell sequencing, resulting in abnormal barcodes that could affect the analysis (called doublets or multilets). Therefore, we used Doublet Finder software to identify and remove double and multiple cells to ensure the quality of the results, with the 7.5% doublet formation rate guideline recommended by 10X Genomics for single-cell analysis, aiming to identify the most likely doublets.

Classification of single-cell clusters

The single-cell subset classification analysis involved several steps. First, low-quality cells were removed, and expression values were normalized using the Log Normalize method in Seurat's “Normalization” function. Next, PCA was performed on the normalized expression values to reduce the dimensionality and variables. The top 10 PCs were selected for clustering and subpopulation analyses. Finally, the Seurat software used a graph-theory-based clustering algorithm to divide the cells. This process included constructing a k-nearest neighbor clustering graph based on the Euclidean distance from significant PCs, optimizing intercellular distance weights using the Jaccard similarity and identifying cell clusters using an SNN module-optimized clustering algorithm.

Analysis of marker genes

Seurat used a bimodal likelihood ratio statistical test to analyze differentially expressed genes (DEGs) across various cell populations to identify genes that were upregulated in different clusters. The screening criteria for upregulated genes were as follows: 1) genes expressed in more than 10% of cells in the target or control subpopulations; 2) *P*-value ≤ 0.01; and 3) gene expression fold change (logFC) ≥ 0.26, meaning that the fold increase in gene expression was ≥ $2^{0.26}$.

Cell-type annotation

Cell annotation results were defined using SingleR by employing a reference dataset derived from Mouse RNAseq Data. The correlation between the gene expression profiles of each cell and the dataset was calculated by assigning each cell a corresponding identification category. We also tallied the cell types identified within each cluster and their respective percentages, selecting the cell type with the highest correspondence for each cluster as the cell-type identification result.

Differential gene expression analysis

For differential analysis, the bimod algorithm was chosen, and the following parameters for screening DEGs were used: 1) $P < 0.01$, 2) logFC ≥ 0.26, and 3) the threshold for gene expression in at least one type of cell was 0.1.

Functional enrichment analysis

For the Ḍ significance enrichment analysis, we initially mapped all DEGs that were differentially expressed by various terms. We then calculated the number of genes belonging to each term and used hypergeometric tests to identify Gene Ontology entries significantly

enriched in DEGs compared to the entire genome background. The Kyoto Encyclopedia of Genes and Genomes (KEGG) enrichment analysis followed the same strategy. Enrichment scatter plots and bar charts were generated using OmicStudio tools at https://www.omicstudio.cn/tool.

Cell-cell communication analysis

CellPhoneDB was used to analyze cellular communication by predicting ligand-receptor interactions based on receptor expression in one cell type and ligand expression in another. For each gene, we calculated the percentage of cells expressing and the average expression of genes. Ligand-receptor pairs were included only if the proportion of cells expressing both genes exceeded 10%. For the polymers, the subunit with the lowest average expression represented the receptor in the statistical analysis. We compared all cell types in pairs within the filtered dataset by randomly arranging the cells into a new population with a default of 1000 arrangements. We determined the mean expression of ligands in a randomly arranged cell population and the average expression of receptors in interacting cell types and then calculated their mean. This process was repeated several times to obtain a normal mean distribution. Next, we calculated the actual average number of ligand-receptor pairs in the original cell population. The significance of the receptor-ligand pair was determined by the proportion of the calculated average values equal to or exceeding the actual average. We then sorted the interactions between cell types based on the number of significant ligand-receptor pairs for manual screening of biologically relevant interactions. As CellPhoneDB only recognizes human genes or proteins, we used the Ensemble tool to convert genes into their homologous counterparts before conducting further analyses.

Results

ScRNA-seq and clustering analysis

We used 10X Genomics technology to analyze the mRNA levels of individual cells isolated from the frontal cortex of rats (Figure 1a). We analyzed 98,338 individual cells from 10 different biological samples. A clear boundary between cells and non-cells was visible. The environmental background was very clean, with almost no environmentally free RNA (Figure 1b). We eliminated cells with potential double droplets, characterized by an unusually high number of detected genes, and unhealthy cells with typical mitochondrial mRNA loads exceeding 10%.

[Figure 1 near here]

Cells were isolated from two groups of 10 tissue samples (n = 5 per group), a blank control group (CON) and a specific mode EA stimulation group (EA). The cells were clustered using the Seurat package, and the t-distributed Stochastic Neighbor Embedding algorithm was used for visualization. Twenty-three clusters (cluster 0–cluster 22) were obtained by cell subgroup classification. The proportion of each cluster in the CON and EA groups is shown in Figure 1c and d.

Identification of cell types in different clusters in the CON and EA groups

The SingleR package was used to identify the predominant cell types. Cells were annotated according to the expression of canonical cell class markers (Figure 2a). We identified eight cell types (Figure 2b). In addition to endothelial cells, we identified astrocytes, microglia, oligodendrocytes, T cells, border-associated macrophages (BAMs), fibroblasts, and granulocytes in this dataset (Figure 2a and b). The combined analysis of cell clustering (Figure 1d) and cell identification showed that endothelial cells were enriched in two subpopulations, astrocytes were enriched in six subpopulations, and microglial marker genes

were enriched in 10 subpopulations. Oligodendrocytes, T cells, BAMs, fibroblasts, and granulocytes each exhibited a single subcluster (Figure 2b and c).

[Figure 2 near here]

Evaluation of DEGs and pathways related to EA intervention on a holistic level

Based on the differences between the EA and CON groups, the cells with large clustering differences between the groups and those closely related to the composition and function of the BBB (endothelial cells, astrocytes, and microglia) were selected for differential analysis to further analyze the mechanism of EA intervention in the BBB.

Endothelial cells

Endothelial cells play a crucial role in BBB function. These cells create a continuous network of tight and adhesive connections along their contacts, forming a selective barrier that regulates the movement of substances inside and outside the brain. The DEGs were analyzed to identify important genes and pathways involved in maintaining this barrier. The expression of a total of 147 genes was significantly increased, and that of 160 genes was markedly downregulated (logFC = 0.26, $P < 0.01$). The expression fold changes of the top 10 genes most significantly upregulated and downregulated are shown in Figure 3a, and all DEGs are listed in Supplementary File 1.

[Figure 3 near here]

To perform enrichment analysis to evaluate the functionality of the 307 genes, we used the Gene Ontology (GO) terms, which encompassed biological processes (BPs), cellular components (CCs), and molecular function (MF), demonstrating the enrichment of 42 GO terms related to the BBB ($P < 0.05$, count ≥ 3) (Figure 3c). KEGG analysis yielded nine pathways that may be associated with BBB function: tight junctions, endocytosis, focal

adhesion, the phosphatidylinositol 3-kinase (PI3K)/Akt signaling pathway, the mitogen-activated protein kinase (MAPK) signaling pathway, the hypoxia-inducible factor 1 (HIF-1) signaling pathway, the Janus kinase/signal transducer and activator of transcription (JAK/STAT) signaling pathway, ferroptosis, and cell adhesion molecules (Figure 3b). Computational gene set enrichment analysis ($q < 0.05$) revealed eight significantly enriched unique pathways and identified the following BPs as being affected by EA: complement and coagulation cascades, ribosomes, lysosomes, cardiac muscle contraction, the rig I-like receptor signaling pathway, proteasomes, antigen processing and presentation, and cytokine-cytokine receptor interactions (Figure 4).

[Figure 4 near here]

DEGs in astrocytes

DEG analysis identified 24 downregulated and three upregulated genes, and the top 10 most upregulated and top three most downregulated genes are shown in Figure 5a. GO was performed. KEGG analyses revealed that DEGs were mainly enriched in calcium-related terms, adenosine triphosphate (ATP) and adenosine diphosphate synthesis and metabolism, and the nicotinamide adenine dinucleotide dehydrogenase complex. These molecules are prominent in certain pathways that may be connected to BBB function and permeability, including positive regulation of vascular permeability, cellular response to the vascular endothelial growth factor stimulus, endothelial cell chemotaxis, and the platelet-derived growth factor receptor signaling pathway (Figure 5b and c). Furthermore, these molecules were also involved in the regulation of the metabolic process of reactive oxygen species, the response to hypoxia, the response to hyperoxia, cell respiration, and the regulation of gaseous respiratory exchange.

[Figure 5 near here]

DEGs in the microglia following EA intervention

Among the DEGs observed in the microglia under EA intervention, the top 10 genes that were most significantly upregulated and downregulated are shown in Figure 6a. EA produced an immediate damage-associated molecular pattern response and the co-chaperone of the heat shock protein 70, DNAJ protein family (Dnaja1 and Dnajb1), related to the inflammatory response (Cao et al., 2014; Kovacs et al., 2017). According to the GO analysis, the terms associated with DEGs were mainly classified into five categories: calcium signaling, MAPK-related pathways, chemokine pathways, extracellular function, and angiogenesis (Figure 6c). Figure 6b shows the results of functional enrichment in the KEGG pathway database, which may be related to BBB function: the MAPK signaling pathway, endocytosis, HIF-1 signaling pathway, PI3K-Akt signaling pathway, tumor necrosis factor (TNF) signaling pathway, cell adhesion molecules, Wnt signaling pathway, and tight junctions.

[Figure 6 near here]

Endothelial cell subsets following EA intervention

Characteristic gene expression of EC_Clusters

The single-cell analysis identified 23 EC subgroups, of which four clusters (clusters 0, 2, 4, and 5) were dominant between the EA and control groups (Figure 7a). Therefore, further GO and KEGG analysis was performed to evaluate the characteristic gene expression patterns of these four subgroups (Figure 7c–f), and the bubble maps of the top 10 genes expressed in these four subgroups are shown in Figure 7b.

[Figure 7 near here]

The upregulated and downregulated genes in these four subgroups were further analyzed (EA vs. CON). The enriched pathways of DEGs in EC_Cluster0 and EC_Cluster2

exhibited a high degree of overlap (Figure 7c and d) and included infectious disease, the immune system, the MAPK signaling pathway, fluid shear stress, and atherosclerosis. In contrast, cluster 0 was enriched in platelet activation, whereas cluster 2 was enriched in the TNF signaling pathway genes. GO and KEGG results showed that the characteristic expression genes of EC_Cluster4 were mainly involved in immune system-related terms (Figure 7e). Similarly, the DEGs of EC_Cluster5 are primarily enriched in pathways related to the immune system, infectious diseases, and the regulation of cell population proliferation. (Figure 7f). In contrast to EC_Cluster4, EC_Cluster5 was also enriched in the interleukin (IL)-17 signaling pathway, fluid shear stress, and the atherosclerosis pathway.

Electroacupuncture altered EC_Clusters of interest

To examine the DEGs and pathways associated with EA exposure from the four subsets of EC, we compared the significantly upregulated or downregulated genes between the EA and CON groups and identified the most representative enriched pathways and processes (Supplementary Files 2 and 3). Neither the upregulated nor downregulated genes of EC_Cluster0 were independent of other clusters; that is, the differential genes of EC_Cluster0 represented the common influence of EA intervention, suggesting that this is the basic response of endothelial cells to the effect of EA.

Thirty-four genes were significantly upregulated, and 11 genes were significantly downregulated by EA in EC_Cluster0 (Supplementary File 2b). Pathway analysis revealed downregulation of cellular responses to extracellular stimuli and inflammatory responses (Supplementary Files 1, 2a and 2d). Genes in pathways that involve leukotriene biosynthetic processes, metabolic processes, and synthase activity were downregulated (Supplementary File 1). We found that EA-related genes related to interferon signaling were upregulated by EA (Supplementary Files 2b and 4), which affects brain endothelial function and barrier

integrity (Oshima et al., 2001; Zhang et al., 2005; Mbofung et al., 2017). Interestingly, Stip1 regulated the Hsp90ab1 function (Li et al., 2014), and its mRNA was also regulated by EA in EC_Cluster0 (Supplementary File 4). Notably, *Hsp90b1* and *Hsp90ab1* were enriched in the fluid shear stress and atherosclerosis pathways (Supplementary File 2c).

The upregulated genes and corresponding functions of EC_Cluster2 were highly correlated with those of EC_Cluster0, with the addition of increased *Psap*, *Mt-co3*, *Pdia4*, and *Atrx.1* expression (Supplementary Files 2g, h, j, and 5a) related to the extracellular matrix region and active transmembrane transporter activity (Supplementary File 6). Only 20 genes were downregulated in EC_Cluster2 (Supplementary File 5b). Among them, *Nfkbia*, *Cxcl10*, and *Cxcl2* had the highest number of enriched pathways, mainly including the NF-κB signaling pathway, IL-17 signaling pathway, TNF signaling pathway, cytokine-cytokine receptor interaction, and chemokine signaling pathway (Supplementary Files 2f, g, i, and 7).

After EA intervention, 15 unique upregulated genes and 13 downregulated genes were identified in EC_Cluster4 (Supplementary File 5). Importantly, downregulated gene enrichment analysis identified pathways related to BBB transport and barrier function. We also observed that terms and pathways related to the immune response were enriched (Supplementary Files 3a, 3b, 3d, and 8). The upregulated DEGs were mainly related to the inflammatory response and involved a variety of cytokine-related signaling pathways. Simultaneously, several typical signaling pathways were also observed, including the ERK cascade, MAPK, and PI3K pathways. Finally, the EA intervention in EC_Cluster4 also resulted in changes in vasculogenesis, astrocyte cell migration, pinocytosis, and calcium-mediated signaling (Supplementary Files 3b, 3c, 3e, and 9).

Among the downregulated genes in EC_Cluster5, only six genes overlapped with other subgroups, and the remaining 104 genes were downregulated (Supplementary File 5b). The downregulated genes were primarily related to ribosomes, suggesting active changes in

protein synthesis and processing (Supplementary File 10). Among the upregulated genes in EC_Cluster 5, 21 coincided with other subgroups, and the remaining 44 genes (Supplementary File 5a) were enriched in the regulation of the establishment of the BBB, sodium-dependent organic anion transmembrane transporter activity, and sprouting, which are important for BBB formation and material transport, in addition to chemokine activity and immune cell chemotaxis (Supplementary Files 3g, 3h, 3j, and 11).

Nature of the microglial cell subsets and the effects of the EA intervention

Analysis of the microglial cell subsets yielded 15 cluster subsets, and marker genes showed different microglial subsets (Supplementary File 12); therefore, these 15 clusters were considered distinct clusters of microglial cells. We selected six clusters (MG_Cluster0, 1, 2, 3, 5, and 6) with large changes and annotated marker genes that were differentially expressed among these cell populations. GO annotation identified the top 20 enrichment terms with the most significant enrichment, whereas KEGG revealed the top 20 pathways with the largest number of genes and the 20 pathways with the smallest *P*-values. A Venn diagram displays the overlap between these pathways and entries (Supplementary Files 13 and 14).

Characteristic DEGs of MG_Clusters

The BP, CC, and MF pathways with the most significant (minimum Q-value) enrichment of the top gene of MG_Cluster1, as well as the top 20 pathways with the highest number of these genes, are displayed in Supplementary Files 13b, 14b, and 15–17. These entries involved the membrane dynamics, G protein-coupled receptor signaling pathway, cytokine-mediated signaling pathway, and extracellular space (Supplementary Files 13, 14a, and 15). KEGG analysis showed cytokine-cytokine receptor interaction, arachidonic acid metabolism, ECM-receptor interaction, signaling pathways regulating stem cell pluripotency, platelet

activation, and JAK-STAT signaling (Supplementary Files 13b, 14b, 14c, 16, and 17). The uniquely enriched entries and pathways of MG_Cluster0 were mainly related to the intracellular anatomical structure, responses of cells to various cytokines, and regulation of transcription factors (Supplementary Files 13a, 14a, and 18). The important pathways were the FoxO and NF-κB signaling pathways (Supplementary Files 13a, 14b, 14c, 18, and 19). In contrast to the other clusters, the functions of MG_Cluster2 included the extracellular region, cellular response to organic substances, and lysosome and chemokine signaling pathways (Supplementary Files 13c, 14, 20–23). MG_Cluster3 had important functions that differed from those of the other clusters, summarized as negative regulation of amyloid fibril formation, positive regulation of tau protein kinase activity, and low-density lipoprotein particle receptor binding (Supplementary Files 13d, 14a, and 24). The total number of entries and pathways representing the unique functions of MG_Cluster5 was the largest (Supplementary File 14), and its functions mainly focused on the immune response (Supplementary Files 13e, 14a–c, 25–27). For MG_Cluster6, the top enriched pathways in MG_Cluster6 were not unique to other clusters (Supplementary Files 14b, 14c, 27–29), and GO enrichment analysis showed that they were mainly related to ATP binding, transcription, and protein folding (Supplementary Files 13f, 14b, 14c, and 28).

DEGs following electroacupuncture intervention in the MG_Clusters

We analyzed the coincidence and non-coincidence of the upregulated and downregulated DEGs in the six clusters (Supplementary Files 30a and 31a). Similarly, we performed an intersection analysis of GO entries with more than two DEGs and KEGG pathways with a Q-value ≤ 0.05 (Supplementary Files 30b, 31b, 31l).

Upregulated genes and enrichment analysis of MG_Clusters

Regarding the quantity of upregulated genes, MG_Cluster3 had the highest number (*n* = 52), followed by MG_Cluster6 (*n* = 38); the numbers in MG_Cluster5 and MG_Cluster0 were 14 and 13, respectively; the number in MG_Cluster2 was seven, while the number in MG_Cluster1 was only one (Supplementary File 30a). In contrast, GO analysis showed that MG_Cluster5 had the largest number of entries, independent of the other clusters (*n* = 53), followed by MG_Cluster6 and MG_Cluster0, with 18 and 13 entries, respectively. MG_Cluster2, MG_Cluster1, and MG_Cluster3 had similar numbers of independent enrichment entries; MG_Cluster2 had eight entries, and the remaining two clusters had seven entries (Supplementary File 30b). Regarding the KEGG pathways, for MG_Cluster0, all activated pathways were similar to those of the other clusters. In contrast, the number of upregulated gene enrichment pathways in MG_Cluster1 that do not overlap with other clusters was the largest (13 pathways). The enrichment of upregulated genes in MG_Cluster6 occurred in six pathways, whereas the featured pathways in MG_Cluster5, 3, and 2 were 3, 2, and 1, respectively (Supplementary File 30i).

Next, based on the above results, we analyzed the unique GO and KEGG enrichment of the six clusters of interest to study the functional changes in each cluster after the EA intervention. Among them, MG_Cluster0 was related to vascular function. MG_Cluster0 functioned as a focal adhesion and synapse (Supplementary File 30c). GO enrichment in MG_Cluster1 was mainly related to post-translational modifications of proteins. The KEGG results showed that Hsp90aa1 and Hsp90ab1 were also enriched in the PI3K/Akt signaling pathway (Supplementary File 30d and j). In MG_Cluster2, we identified genes upregulated in the cluster after EA intervention, which involved the basement membrane and extracellular region (Supplementary File 30e and j). Upregulated genes in MG_Cluster3 were mainly enriched in GO terms related to axon and myelin. KEGG analysis revealed that this cluster was related to ribosomes (Supplementary File 30f and j). In MG_Cluster5, the upregulated

genes were mainly enriched in the cytosol and plasma membrane. Notably, the two genes upregulated in the cluster (*Ccl3* and *Ccl4*) play key roles in and are mainly enriched in calcium and CCR chemokine receptor-related functions, as well as in the toll-like receptor signaling pathway (Supplementary File 30g and k). The enriched pathways in MG_Cluster6 are mostly related to mitochondria after EA intervention (Supplementary File 30h and k).

Downregulated genes and enrichment analysis of MG_Clusters

We observed that among the six clusters of independently downregulated genes, MG_Cluster3 and MG_Cluster6 involved far more genes than the other clusters, with 82 and 68 genes, respectively. The number of pathways identified in the GO and KEGG enrichments of MG_Cluster6 were also higher than those of the other five clusters (Supplementary File 31a, b, and l), including the cellular response to various stimuli. Another noteworthy pathway was the fluid shear stress and atherosclerosis pathway (Supplementary File 31h and k), because the fluid shear stress generated by directional shear of blood flow directly acts on brain microvascular endothelial cells.

Furthermore, the downregulated genes in MG_Cluster0 were mainly associated with focal adhesion, synapses, the response to angiotensin, and positive regulation of angiogenesis; however, no unique KEGG enrichment pathway was identified (Supplementary File 31c). The G protein-coupled purine nucleotide receptor and platelet activation were the key terms of MG_Cluster1 enriched (Supplementary File 31d and j). In the GO enrichment of MG_Cluster2, nine important genes were downregulated (Supplementary File 31g and l). In the unique GO of MG_Cluster3, we focused on the regulation of T cell and B cell migration. KEGG analysis yielded three pathways, including inositol phosphate metabolism, the C-type lectin receptor signaling pathway, and the phosphatidylinositol signaling system

(Supplementary File 31e and l). Finally, the MG_Cluster5 downregulated genes enriched GO terms and pathways were mainly related to immune function (Supplementary File 31f and l).

Coordination of cell communication in the BBB following EA intervention

Because the BBB is orchestrated by the coordinated actions and interactions of several different cell types, cell communication analysis is necessary. First, we compared cell communication between the EA and CON groups (Supplementary File 32a–f) and further investigated the communication network between the two groups of cells and other cells (Supplementary File 32g and h). The number of protein interactions between the different cell types ($P < 0.05$) was calculated to generate a heat map (Supplementary File 32a and d), and the heat map values were log (natural logarithm) log-transformed (Supplementary File 32e and f). Since endothelial cells are the most direct cell type constituting the physical characteristics of the BBB, we focused on the degree of communication between various types of cells and endothelial cells. Upon comparing the EA and CON groups, we found that BAMs, microglia (MG), T cells, granulocytes, and endothelial cells demonstrated obvious differences in their interactions with endothelial cells (Supplementary File 32a and d). The results suggested that the cells with the most active relationship with endothelial cells were astrocytes, fibroblasts, and endothelial cells, whereas the largest changes between the two groups were granulocytes (GC) (Supplementary File 32b, e, g, and h).

To further explore the interaction between cell types, we analyzed the ligand-receptor pairs of other cells interacting with endothelial cells (Supplementary File 33a). Among the top 20 ligand-receptor pairs in the mean value, there were four pairs of interactions with endothelial cells that were different between the groups, namely CD74_APP, PLXNB2_PTN, LAMP1_FAM3C, and CD74_COPA. TNFRSF21_APP was present only in the CON group, whereas CSF1R_CSF1 was specifically present in the EA group (Supplementary File 33a). In

the CON group, the ligand-receptor pair CD74_APP was not observed, suggesting that the EA intervention activated the ligand-receptor interaction of CD74_APP. In the communication between the AC and the EC, the ligand-receptor pair activated by the EA also contained TNFSF12_TNFRSF25, while GDF11_TGFR_AVR2B was blocked. Additionally, the mean interactions of TYRO3_GAS6, TNFSF13_TNFRSF1A, NOTCH1_JAG2, FGFR2_EPHA4, and FGFR2_PTPRR were consistently decreased in the EA group (Supplementary File 33b). The FB-EC communication attracted our attention because there were more ligand-receptor pairs than others. In the EA group, the communication between TGFB3 in the FB and its corresponding receptors in the endothelial cells was activated. Furthermore, apart from the higher mean PLXNB2_PTN in the EA group than that in the CON group, we observed that all other ligand-receptor pairs with mean changes were higher in the CON group (Supplementary File 33c).

Except for the TNFSF12_TNFRSF25 exclusively in the EA group and PLXNB2_SEMA4C in the CON group, in the ligand-receptor interaction between microglia and EC, we observed nine pairs of ligand-receptor pairs promoted by EA (Supplementary File 33d). In terms of interaction between granulocytes and endothelial cells (GC-EC), many ligand-receptor pairs were present only in the EA or CON group (Supplementary File 33e). We then focused on oligodendrocyte and endothelial cell (OC-EC) communication and found that the *P*-values of most ligand-receptor pairs decreased in the EA group, suggesting that EA rendered these interactions more pronounced. In addition, there were also communications that appeared exclusively in one group (Supplementary File 33f). In terms of the TC and EC communication, TGFB1_TGFbeta_receptor1 and TGFB1_TGFbeta_receptor2 appeared only in the EA group, whereas AR_Testosterone_byHSD17B12, COL11A2_integrin_a1b1_complex, IFNG_Type_II_IFNR, and SEMA4A_PLXND1 were only present in the CON group. The *P*-value of TGFB1_TGFBR3 was smaller in the EA

group, while the *P*-value of CXCR6_CXCL16 was smaller in the CON group, and three pairs had a larger mean in the EA group (Supplementary File 33g). Finally, EA activated the communication of JAG1_NOTCH4 and TNFSF12_TNFRSF25 and blocked the communication of IGFBP3_TMEM219 and MERTK_GAS6 in BAM-endothelial cells (Supplementary File 33h).

Discussion

Increased expression of inflammatory markers such as C-C motif chemokine ligand (CCL-4 and CCL-3) and TMEM119 and decreased expression of cellular communication network family proteins results in increased BBB permeability (Lee et al., 2017; You et al., 2019; Davidson et al., 2022; Liu et al., 2022; Liu et al., 2024). Previous studies have shown that the AAV-PHP.eB delivery is facilitated by the receptor protein lymphocyte antigen-6E (LY6E) in humans (Fu et al., 2021). EA pretreatment reduces BBB permeability and upregulates the expression of *Irf7* in healthy rats (Wu et al., 2019). Moreover, functional analysis in our study identified numerous terms and pathways associated with the BBB. Unexpectedly, the large clustering differences in microglia with and without EA intervention caught our attention. Indeed, microglia may serve as crucial priming cells for EA-induced opening of the BBB. Consequently, future research could focus on this aspect, and our laboratory is currently investigating this phenomenon, even though current research on microglia and BBB is mostly focused on the pathology and neuroinflammation of neurodegenerative diseases (Xu et al., 2015).

Higher basal Hmox1 expression in microglia is accompanied by increased oxidative stress, which directly affects the permeability of the BBB. Furthermore, Hmox1 regulates microglial polarization to the M2 phenotype (Groh et al., 2023). Of the top 10 genes that were downregulated after EA treatment, *Mx1*, *Mx2*, *Ifi27*, and *Ly6e* are immune-related

genes, while Iba1 (encoded by *Aif1*) is a canonical microglial marker (Gandal et al., 2018). In addition, Pycard and Ltc4s function as mediators in apoptosis and inflammation (McConnell and Vertino, 2000; Agostini et al., 2004; Faustin et al., 2007; Fernandes-Alnemri et al., 2007; Bryan et al., 2009; Hasegawa et al., 2009; Hornung et al., 2009; Taxman et al., 2011; Lu et al., 2014; Guan et al., 2015; Shen et al., 2019; Shen et al., 2021).

The relationship between FK506 binding protein (FKBP) and the immunosuppressive drug FK506 has been examined; FKBP5 and FKBP4 are associated with neurological diseases, including Parkinson's disease and AD (McConnell and Vertino, 2000; Bryan et al., 2009; Jiang et al., 2023). Notably, the basic neural basis synapses of memory and cognitive function are highly susceptible to synaptic phagocytosis by activated microglia and may improve cognitive function by reducing excessive activation of microglia (Reverte et al., 2024). We also observed enrichment of the pathway associated with cocaine addiction, which has been associated with microglia for synaptic adaptations in the nucleus accumbens synapses during cocaine withdrawal (Victor et al., 2022). Another pathway, thyroid hormone synthesis, is important for the microglial phenotype (Supplementary Files 13d, 14b, 14c, 29, and 34). The trigger receptor expressed in myeloid cell 2 (TREM2) is a cell surface receptor found in macrophages and microglia that responds to disease-related signals to regulate the phenotype of these innate immune cells. TREM2 is regulated by thyroid hormones, and its expression in macrophages and microglia is stimulated by thyroid hormones and synthetic thyroid hormone agonists (thyroid inhibitors).

In addition to considering the overall clustering of endothelial cells and microglia, which are cells with large differences in clustering, subsequent experiments should also focus on changes in the characteristics of the clustering of these cell subpopulations to explore whether there are certain unknown potential key subpopulations that play a critical role in BBB permeability. Similarly, cell communication analysis should not be confined to

astrocytes and pericytes, which are typically regarded as cell types that are functionally associated with the BBB or comprised in the BBB. Differences in clustering and gene expression were also present in fibroblasts, BAMs, and T cells, although not so pronounced as to be focused on in this article, but it is possible that they are also involved in the regulation of BBB permeability.

This study had some limitations. First, as this investigation represents the initial analysis of single-cell transcriptome sequencing in the frontal cortex following EA intervention, there exists a limited understanding of the signaling pathways involved in EA-mediated BBB function. Second, a rat model was selected for this study due to considerations of EA operational precision. Third, additional protein analyses and functional validation are necessary to confirm the putative roles of each cellular phenotype. Finally, the possibility cannot be excluded that certain cells or cell types may be lost during tissue dissociation and cell enrichment; indeed, pericytes and neurons, which also play significant roles in the brain, were not enriched in this study. Nevertheless, this single-cell transcriptome sequencing in a rat model to investigate the target of action of EA-opening BBB could facilitate the study of BBB-opening-related mechanisms, which is crucial to numerous current investigations of exogenous drugs crossing the BBB into the brain.

Conclusions

The study of the molecular and cellular mechanisms that govern the function of the BBB is complex and requires a thorough understanding of the classification and molecular characteristics of cells, as well as detailed characterization of the spatial organization and interaction of molecularly defined cell types. This is because the spatial relationship between cells is the primary determinant of intercellular interactions and communication, which are mediated by juxtacrine and paracrine signaling. Our study revealed a unique frontal cortex-

specific transcriptome signature and elucidated the cell types and clusters that mediate EA-induced transcriptional changes, including cellular communication. Our study highlights the characteristic changes in brain endothelial cells under EA intervention, as well as the cell types that synergistically participate in the structural and functional changes of the BBB, such as microglia and astrocytes, providing a framework for the mechanism of EA opening the BBB. The development of high-resolution, spatially resolved whole-brain cell atlases will provide invaluable resources for investigating BBB function during EA interventions. Future research in this area is necessary to elucidate the intricate details of intercellular communication and gain a deeper understanding of the mechanisms underlying BBB function.

Declarations

Ethics approval and consent to participate: The Animal Ethics Committee of Zhejiang Chinese Medical University approved the experimental procedures (Approval No.: IACUC-20220507-01). All experiments were performed in accordance with the ARRIVE guidelines. Consent to participate was not applicable.

Consent for publication: Not applicable.

Availability of data and materials: This study did not generate new unique reagents. The scRNA-seq data files are publicly available in the Gene Expression Omnibus (https://www.ncbi.nlm.nih.gov/geo/query/acc.cgi?acc=GSE272895) under accession number GSE272895.

Competing interests*:* The authors declare that they have no competing interests.

Authors' contributions: C.M.: Conceptualization, Data curation, Funding acquisition, Writing – original draft, and Visualization. Z.J., L.G., K.Q., and T.J.: Validation, Software, and Resources. J.Y., Z.P., and Q.C.: Project administration and Formal analysis, and M.D. and Q.Y.: Investigation and Methodology. X.L.: Funding acquisition and Writing – review & editing. All authors read and approved the final manuscript.

Acknowledgments: We appreciate the support of the Key Laboratory of Acupuncture and Neurology of Zhejiang Province and the technical support from the Medical Research Center, Academy of Chinese Medical Sciences, Zhejiang Chinese Medical University. We thank Mr. Xushen Chen of the School of Public Health, Zhejiang Chinese Medical University, for his help with the language. We would also like to thank Editage (www.editage.cn) for English language editing.

References

Agostini L, Martinon F, Burns K, McDermott MF, Hawkins PN, Tschopp J. NALP3 forms an IL-1beta-processing inflammasome with increased activity in Muckle-Wells autoinflammatory disorder. Immunity. 2004;20:319–25. doi:10.1016/s1074-7613(04)00046-9.

Bryan NB, Dorfleutner A, Rojanasakul Y, Stehlik C. Activation of inflammasomes requires intracellular redistribution of the apoptotic speck-like protein containing a caspase recruitment domain. J Immunol. 2009;182:3173–82. doi:10.4049/jimmunol.0802367.

Cao M, Wei C, Zhao L, Wang J, Jia Q, Wang X, et al. DnaJA1/Hsp40 is co-opted by influenza A virus to enhance its viral RNA polymerase activity. J Virol. 2014;88:14078–89. doi:10.1128/JVI.02475-14.

Chi Z, Chen S, Yang D, Cui W, Lu Y, Wang Z, et al. Gasdermin D-mediated metabolic crosstalk promotes tissue repair. Nature. 2024;634:1168–77. doi:10.1038/s41586-024-08022-7.

Dai M, Qian K, Ye Q, Yang J, Gan L, Jia Z, et al. Specific mode electroacupuncture stimulation mediates the delivery of NGF across the hippocampus blood-brain barrier through p65-VEGFA-TJs to improve the cognitive function of MCAO/R convalescent rats. Mol Neurobiol. 2025;62:1451–66. doi:10.1007/s12035-024-04337-8.

Davidson M, Mayer M, Habib A, Rashidi N, Filippone RT, Fraser S, et al. Methamphetamine induces systemic inflammation and anxiety: the role of the gut-immune-brain axis. Int J Mol Sci. 2022;23:11224. doi:10.3390/ijms231911224.

Faustin B, Lartigue L, Bruey JM, Luciano F, Sergienko E, Bailly-Maitre B, et al. Reconstituted NALP1 inflammasome reveals two-step mechanism of caspase-1 activation. Mol Cell. 2007;25:713–24. doi:10.1016/j.molcel.2007.01.032.

Fernandes-Alnemri T, Wu J, Yu JW, Datta P, Miller B, Jankowski W, et al. The pyroptosome: a supramolecular assembly of ASC dimers mediating inflammatory cell death via caspase-1 activation. Cell Death Differ. 2007;14:1590–604. doi:10.1038/sj.cdd.4402194.

Fu S, Yu M, Xu H, Liu Q, Li X, Wang Y, et al. Genome-wide transcription analysis of electroacupuncture precondition-induced ischemic tolerance on SD rat with ischemia-reperfusion injury. Front Genet. 2021;12:719201. doi:10.3389/fgene.2021.719201.

Gandal MJ, Haney JR, Parikshak NN, Leppa V, Ramaswami G, Hartl C, et al. Shared molecular neuropathology across major psychiatric disorders parallels polygenic overlap. Science. 2018;359:693–7. doi:10.1126/science.aad6469.

Groh J, Abdelwahab T, Kattimani Y, Hörner M, Loserth S, Gudi V, et al. Microglia-mediated demyelination protects against CD8+ T cell-driven axon degeneration in mice carrying PLP defects. Nat Commun. 2023;14:6911. doi:10.1038/s41467-023-42570-2.

Guan K, Wei C, Zheng Z, Song T, Wu F, Zhang Y, et al. MAVS promotes inflammasome activation by targeting ASC for K63-linked ubiquitination via the E3 ligase TRAF3. J Immunol. 2015;194:4880–90. doi:10.4049/jimmunol.1402851.

Hasegawa M, Imamura R, Motani K, Nishiuchi T, Matsumoto N, Kinoshita T, et al. Mechanism and repertoire of ASC-mediated gene expression. J Immunol. 2009;182:7655–62. doi:10.4049/jimmunol.0800448.

Hornung V, Ablasser A, Charrel-Dennis M, Bauernfeind F, Horvath G, Caffrey DR, et al. AIM2 recognizes cytosolic dsDNA and forms a caspase-1-activating inflammasome with ASC. Nature. 2009;458:514–8. doi:10.1038/nature07725.

Jiang J, Zou Y, Xie C, Yang M, Tong Q, Yuan M, et al. Oxytocin alleviates cognitive and memory impairments by decreasing hippocampal microglial activation and synaptic defects via OXTR/ERK/STAT3 pathway in a mouse model of sepsis-associated encephalopathy. Brain Behav Immun. 2023;114:195–213. doi:10.1016/j.bbi.2023.08.023.

Kovacs ZI, Kim S, Jikaria N, Qureshi F, Milo B, Lewis BK, et al. Disrupting the blood-brain barrier by focused ultrasound induces sterile inflammation. Proc Natl Acad Sci U S A. 2017;114:E75–84. doi:10.1073/pnas.1614777114.

Lee LL, Aung HH, Wilson DW, Anderson SE, Rutledge JC, Rutkowsky JM. Triglyceride-rich lipoprotein lipolysis products increase blood-brain barrier transfer coefficient and induce astrocyte lipid droplets and cell stress. Am J Physiol Cell Physiol. 2017;312:C500–16. doi:10.1152/ajpcell.00120.2016.

Li J, Hou B, Tumova S, Muraki K, Bruns A, Ludlow MJ, et al. Piezo1 integration of vascular architecture with physiological force. Nature. 2014;515:279–82. doi:10.1038/nature13701.

Lin Y, Gan L, Ren L, Ma C, Dai M, Qian K, et al. Acupuncture with specific mode electro-stimulation effectively and transiently opens the BBB through Shh signaling pathway. NeuroReport. 2023;34:873–86. doi:10.1097/WNR.0000000000001970.

Liu D, Zhu M, Lin Y, Li M, Huang R, Yang L, et al. LY6E protein facilitates adeno-associated virus crossing in a biomimetic chip model of the human blood-brain barrier. Lab Chip. 2022;22:4180–90. doi:10.1039/d2lc00698g.

Liu S, Jia X, Liu B, Liu Y, Yin H. Suppression of cerebral ischemia injury induced blood brain barrier breakdown by dexmedetomidine via promoting CCN1. Aging. 2024;16:3750–62. doi:10.18632/aging.205557.

Lu A, Magupalli VG, Ruan J, Yin Q, Atianand MK, Vos MR, et al. Unified polymerization mechanism for the assembly of ASC-dependent inflammasomes. Cell. 2014;156:1193–206. doi:10.1016/j.cell.2014.02.008.

Ma C, Gan L, Wang H, Ren L, Lin Y, Zhao Y, et al. Transcriptomic analysis of rat cerebral cortex reveals the potential mechanism of electroacupuncture opening blood brain barrier. Front Neurosci. 2022;16:834683. doi:10.3389/fnins.2022.834683.

Ma C, Ye Q, Qian K, Dai M, Gan L, Yang J, et al. Anti-glioma effect of paclitaxel mediated by specific mode electroacupuncture stimulation and the related role of the Hedgehog pathway. Brain Res Bull. 2024;213:110985. doi:10.1016/j.brainresbull.2024.110985.

Mbofung RM, McKenzie JA, Malu S, Zhang M, Peng W, Liu C, et al. HSP90 inhibition enhances cancer immunotherapy by upregulating interferon response genes. Nat Commun. 2017;8:451. doi:10.1038/s41467-017-00449-z.

McConnell BB, Vertino PM. Activation of a caspase-9-mediated apoptotic pathway by subcellular redistribution of the novel caspase recruitment domain protein TMS1. Cancer Res. 2000;60:6243–7.

Oshima T, Laroux FS, Coe LL, Morise Z, Kawachi S, Bauer P, et al. Interferon-gamma and interleukin-10 reciprocally regulate endothelial junction integrity and barrier function. Microvasc Res. 2001;61:130–43. doi:10.1006/mvre.2000.2288.

Reverte I, Marchetti C, Pezza S, Zenoni SF, Scaringi G, Ferrucci L, et al. Microglia-mediated calcium-permeable AMPAR accumulation in the nucleus accumbens drives hyperlocomotion during cocaine withdrawal. Brain Behav Immun. 2024;115:535–42. doi:10.1016/j.bbi.2023.11.007.

Shen C, Lu A, Xie WJ, Ruan J, Negro R, et al. Molecular mechanism for NLRP6 inflammasome assembly and activation. Proc Natl Acad Sci U S A. 2019;116:2052–7. doi:10.1073/pnas.1817221116.

Shen C, Li R, Negro R, Cheng J, Vora SM, Fu TM, et al. Phase separation drives RNA virus-induced activation of the NLRP6 inflammasome. Cell. 2021;184:5759–74.e20. doi:10.1016/j.cell.2021.09.032.

Taxman DJ, Holley-Guthrie EA, Huang MT, Moore CB, Bergstralh DT, Allen IC, et al. The NLR adaptor ASC/Pycard regulates DUSP10, mitogen-activated protein kinase (MAPK), and chemokine induction independent of the inflammasome. J Biol Chem. 2011;286:19605–16. doi:10.1074/jbc.M111.221077.

Victor MB, Leary N, Luna X, Meharena HS, Scannail AN, Bozzelli PL, et al. Lipid accumulation induced by APOE4 impairs microglial surveillance of neuronal-network activity. Cell Stem Cell. 2022;29:1197–212.e8. doi:10.1016/j.stem.2022.07.005.

Wu X, Fu S, Liu Y, Luo H, Li F, Wang Y, et al. NDP-MSH binding melanocortin-1 receptor ameliorates neuroinflammation and BBB disruption through CREB/Nr4a1/NF-κB pathway after intracerebral hemorrhage in mice. J Neuroinflammation. 2019;16:192. doi:10.1186/s12974-019-1591-4.

Xu L, Dan M, Shao A, Cheng X, Zhang C, Yokel RA, et al. Silver nanoparticles induce tight junction disruption and astrocyte neurotoxicity in a rat blood-brain barrier primary triple coculture model. Int J Nanomedicine. 2015;10:6105–18. doi:10.2147/IJN.S85265.

You M, Miao Z, Pan Y, Hu F. Trans-10-hydroxy-2-decenoic acid alleviates LPS-induced blood-brain barrier dysfunction by activating the AMPK/PI3K/AKT pathway. Eur J Pharmacol. 2019;865:172736. doi:10.1016/j.ejphar.2019.172736.

Zhang J, Lin X, Zhou H, Chen Y, Xiao S, Jiao J, et al. Electroacupuncture: a new approach to open the blood-brain barrier in rats recovering from middle cerebral artery occlusion. Acupunct Med. 2018;36:377–85. doi:10.1136/acupmed-2017-011496.

Zhang S, Gong P, Zhang J, Mao X, Zhao Y, Wang H, et al. Specific frequency electroacupuncture stimulation transiently enhances the permeability of the blood-brain barrier and induces tight junction changes. Front Neurosci. 2020;14:582324. doi:10.3389/fnins.2020.582324.

Zhang Y, Zhang X, Park TS, Gidday JM. Cerebral endothelial cell apoptosis after ischemia-reperfusion: role of PARP activation and AIF translocation. J Cereb Blood Flow Metab. 2005;25:868–77. doi:10.1038/sj.jcbfm.9600081.

Figure Legends

Figure 1. Overview of single-cell analysis of the experimental samples. (a) Schematic overview of the study design. **(b)** Results of effective cell identification. **(c)** Percentage of 23 clusters in EA and CON groups. **(d)** T-Distributed Stochastic Neighbor Embedding (t-SNE) of the transcriptome from cells of the CON and EA groups. CON, control; EA, electroacupuncture.

Figure 2. Results of the cell type identification. (a) Dot plot heatmap of the marker genes in individual clusters. **(b)** Cell type identification T-Distributed Stochastic Neighbor Embedding (t-SNE) diagram. **(c)** The violin plot shows the expression of marker genes of eight cells. CON, control; EA, electroacupuncture.

Figure 3. Differential gene and enrichment analysis results of the endothelial cells. (a) Differential gene volcano map. **(b)** Histogram of the KEGG analysis results. **(c)** Histogram of the GO analysis results. GO, Gene Ontology; KEGG, Kyoto Encyclopedia of Genes and Genomes.

Figure 4. Gene set enrichment analysis results. Eight pathways are shown.

Figure 5. Differential gene and enrichment analysis results of astrocytes. (a) Differential gene volcano map. **(b)** Histogram of KEGG analysis results. **(c)** Histogram of GO analysis results. GO, Gene Ontology; KEGG, Kyoto Encyclopedia of Genes and Genomes.

Figure 6. Differential gene and enrichment analysis results of the microglia. (a) Differential gene volcano map. **(b)** Histogram of KEGG analysis results. **(c)** Histogram of GO analysis results. GO, Gene Ontology; KEGG, Kyoto Encyclopedia of Genes and Genomes.

Figure 7. Subgroup clustering and functional enrichment of endothelial cells. (a) Endothelial cell subset analysis in the two groups. **(b)** The top 10 characteristic expression genes of the four subgroups. **(c–f)** The GO and KEGG results of the characteristic expression genes of the four subgroups. The histogram of GO results show that the number of enriched genes was ranked in the top 20, and $q < 0.05$. The histogram and bubble diagram of the KEGG results show the top 20 terms of the number of enriched genes and the 20 terms with the smallest *P*-value, respectively. GO, Gene Ontology; KEGG, Kyoto Encyclopedia of Genes and Genomes.

Supplementary Files

Supplementary File 1: Pathway analysis for genes downregulated by SMES only in EC_cluster0

Supplementary File 2: Differential gene and enrichment analysis results of EC_Cluster0 and EC_Cluster2, related to Figure 7.

Supplementary File 3: Differential gene and enrichment analysis results of EC_Cluster4 and EC_Cluster5, related to Figure 7.

Supplementary File 4: Pathway analysis for genes upregulated by SMES only in EC_cluster0

Supplementary File 5: Venn diagram showing the differential gene intersection and uniqueness of the four clusters of interest in endothelial cells, related to Figure 7.

Supplementary File 6: Pathway analysis for genes upregulated only in EC_cluster2

Supplementary File 7: Pathway analysis for genes downregulated only in EC_cluster2

Supplementary File 8: Pathway analysis for genes downregulated only in EC_cluster4

Supplementary File 9: Pathway analysis for genes upregulated only in EC_cluster4

Supplementary File 10: Pathway analysis for genes downregulated only in EC_cluster5

Supplementary File 11: Pathway analysis for genes upregulated only in EC_cluster5

Supplementary File 12: Subgroup clustering and functional enrichment of microglia, related to Figure 6.

Supplementary File 13: The GO and KEGG results of the characteristic expression genes of the six subgroups of microglia, related to Figure 6.

Supplementary File 14: Upset map of crossover and uniqueness of the enrichment function of the characteristic genes of 6 MG_Clusters of interest, related to Figure 6.

Supplementary File 15: GO analysis for MG_cluster1 top genes only (S≥2)

Supplementary File 16: KEGG analysis for MG_cluster1 top genes only (counts top 20)

Supplementary File 17: KEGG analysis for MG_cluster1 top genes only (20 smallest P values)

Supplementary File 18: GO analysis for MG_cluster0 top genes only (S≥2)

Supplementary File 19: KEGG analysis for MG_cluster0 top genes only (counts top 20)

Supplementary File 20: KEGG analysis for MG_cluster0 top genes only (20 smallest P values)

Supplementary File 21: GO analysis for MG_cluster2 top genes only (S≥2)

Supplementary File 22: KEGG analysis for MG_cluster2 top genes only (counts top 20)

Supplementary File 23: KEGG analysis for MG_cluster2 top genes only (20 smallest P values)

Supplementary File 24: GO analysis for MG_cluster3 top genes only (S≥2)

Supplementary File 25: GO analysis for MG_cluster5 top genes only (S≥2)

Supplementary File 26: KEGG analysis for MG_cluster5 top genes only (counts top 20)

Supplementary File 27: KEGG analysis for MG_cluster5 top genes only (20 smallest P values)

Supplementary File 28: GO analysis for MG_cluster6 top genes only (S≥2)

Supplementary File 29: KEGG analysis for MG_cluster3 top genes only (counts top 20)

Supplementary File 30: Functional enrichment analysis of unique upregulated genes in MG_clusters after electroacupuncture, related to Figure 6.

Supplementary File 31: Functional enrichment analysis of unique downregulated genes in MG_clusters after EA, related to Figure 6.

Supplementary File 32: The interactions between cells, related to the section "Coordination of cell communication in the BBB following EA intervention."

Supplementary File 33: Cell communication with endothelial cells, related to the section "Coordination of cell communication in the BBB following EA intervention."

Supplementary File 34: KEGG analysis for MG_cluster3 top genes only (20 smallest P values)

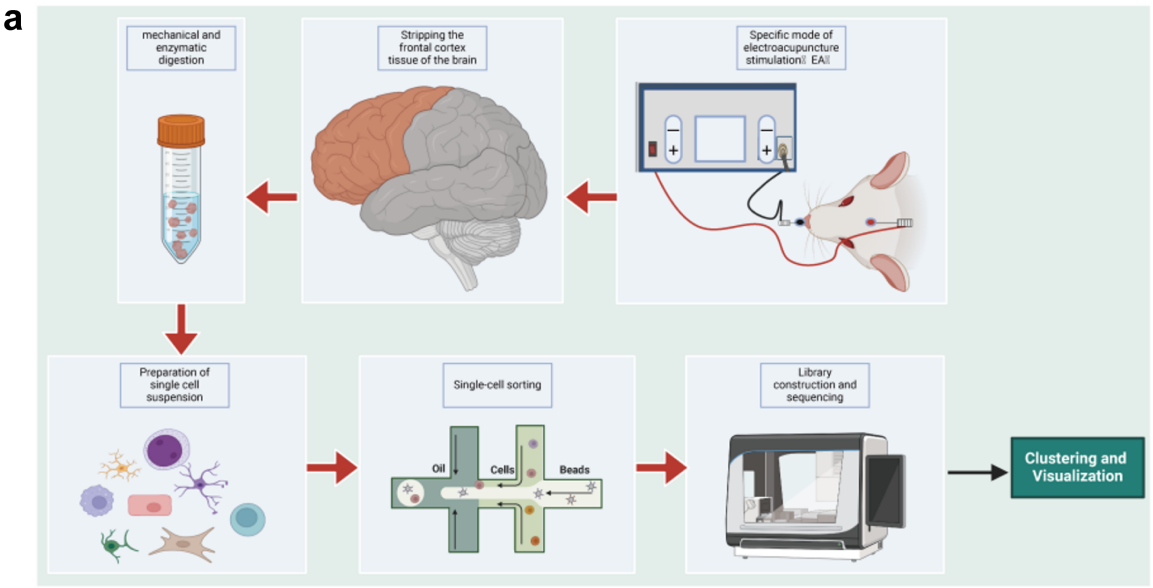
a
mechanical and enzymatic digestion
Stripping the frontal cortex tissue of the brain
Specific mode of electroacupuncture stimulation（EA）
Preparation of single cell suspension
Single-cell sorting
Oil
Cells
Beads
Library construction and sequencing
Clustering and Visualization

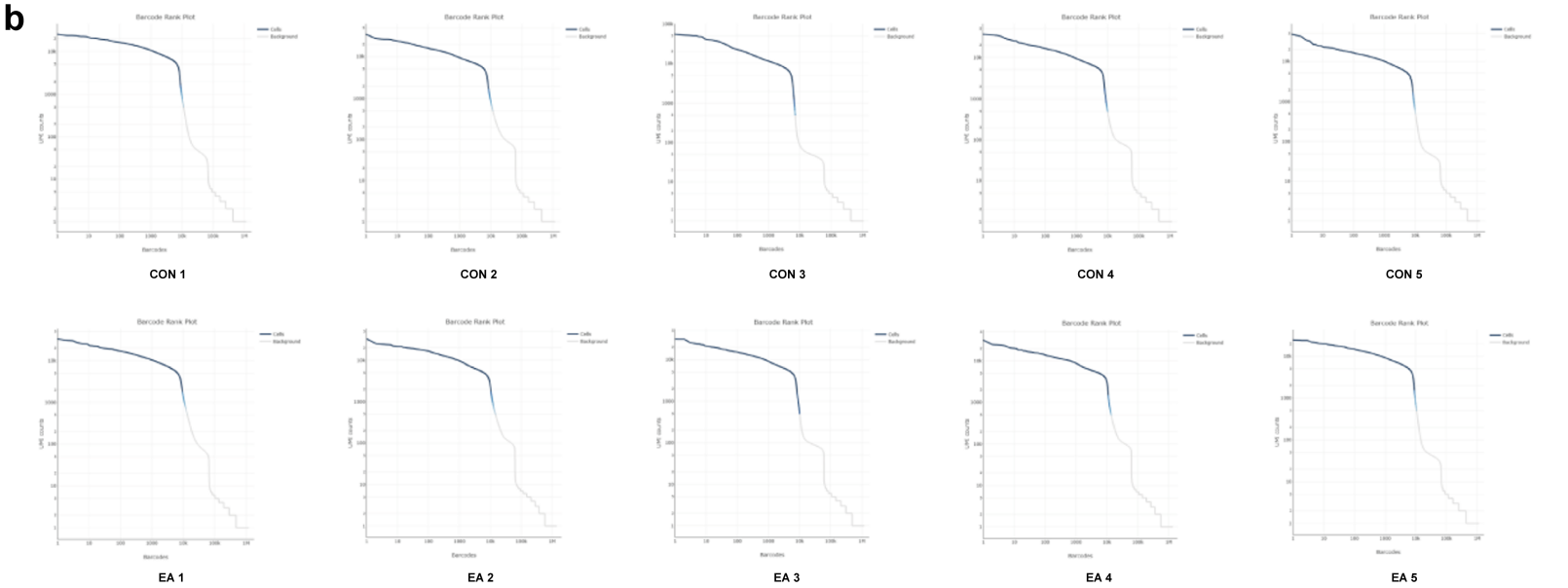
b
Barcode Rank Plot
CON 1
CON 2
CON 3
CON 4
CON 5
EA 1
EA 2
EA 3
EA 4
EA 5

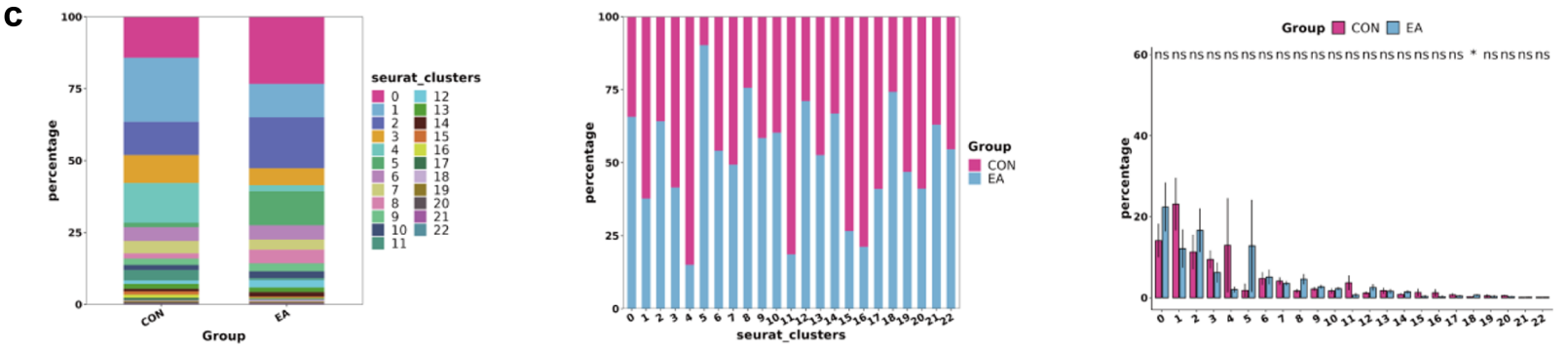
c
percentage
Group
CON
EA
seurat_clusters
Group CON EA
ns ns ns ns ns ns ns ns ns ns ns ns ns ns ns ns ns ns ns ns ns * ns ns ns ns

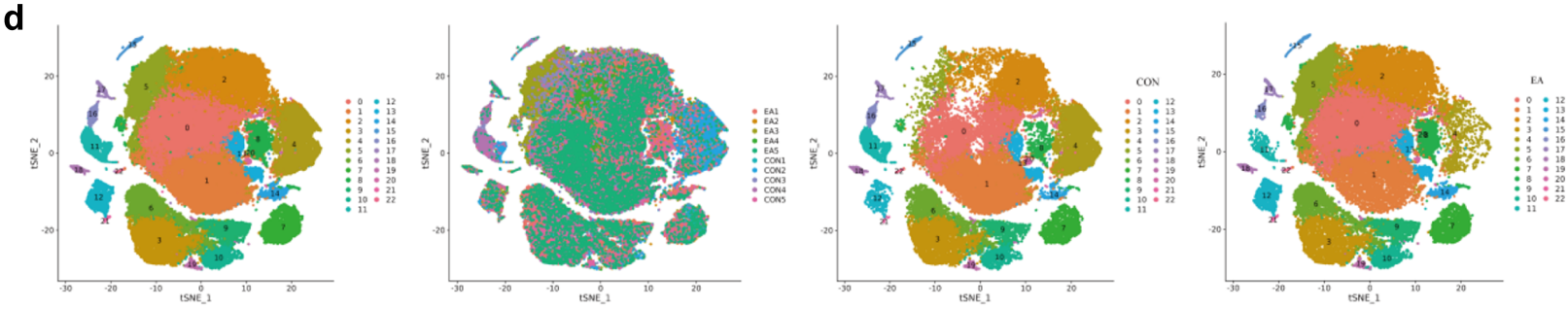
d
tSNE_1
tSNE_2
CON
EA

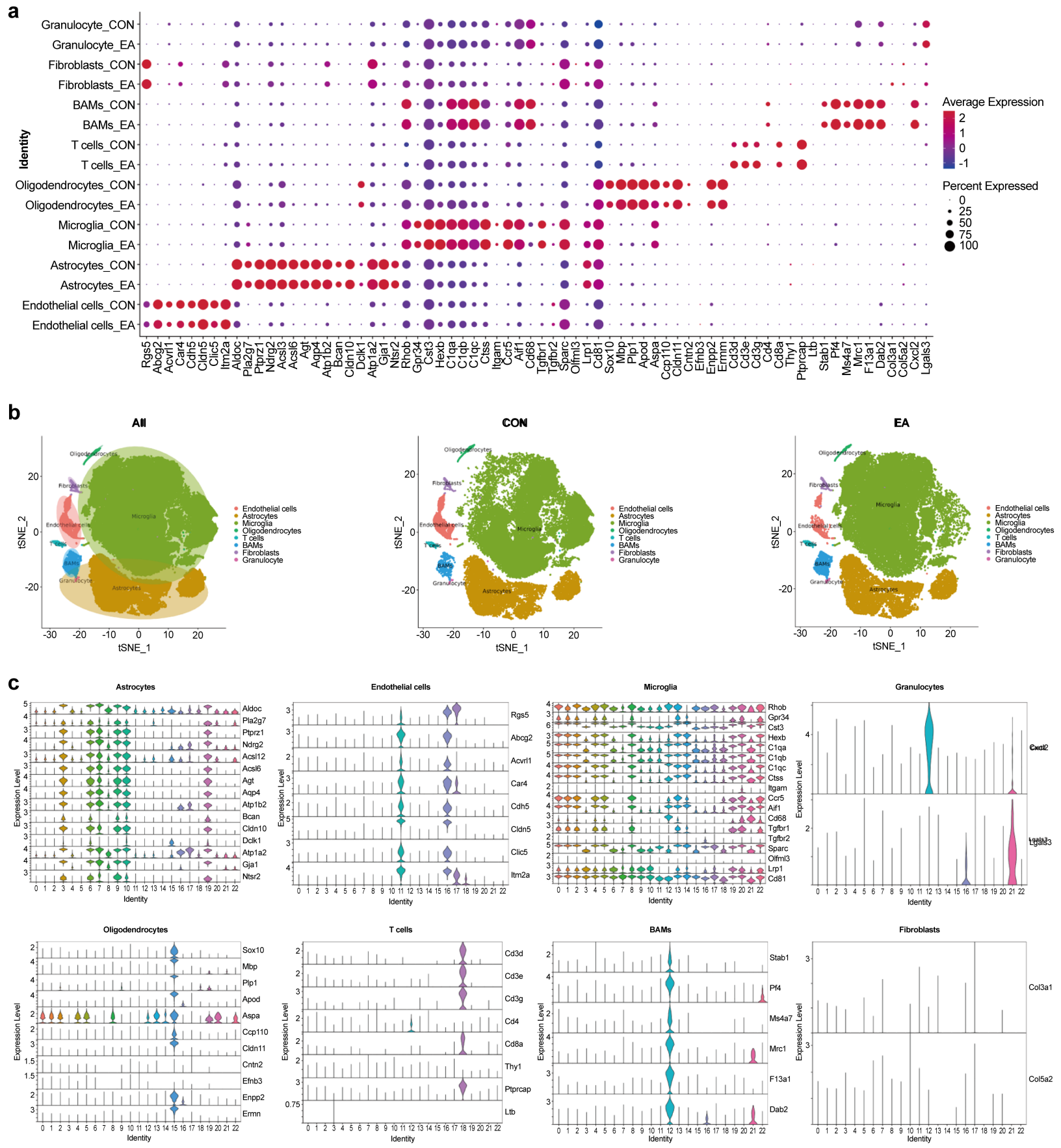
a
Identity
Granulocyte_CON
Granulocyte_EA
Fibroblasts_CON
Fibroblasts_EA
BAMs_CON
BAMs_EA
T cells_CON
T cells_EA
Oligodendrocytes_CON
Oligodendrocytes_EA
Microglia_CON
Microglia_EA
Astrocytes_CON
Astrocytes_EA
Endothelial cells_CON
Endothelial cells_EA
Rgs5 Abcg2 Acvrl1 Car4 Cdh5 Cldn5 Clic5 Itm2a Aldoc Pla2g7 Ptprz1 Ndrg2 Acsl3 Acsl6 Agt Aqp4 Atp1b2 Bcan Cldn10 Dclk1 Atp1a2 Gja1 Ntsr2 Rhob Gpr34 Cst3 Hexb C1qa C1qb C1qc Ctss Itgam Ccr5 Aif1 Cd68 Tgfbr1 Tgfbr2 Sparc Olfml3 Lrp1 Cd81 Sox10 Mbp Plp1 Apod Aspa Ccp110 Cldn11 Cntn2 Efnb3 Enpp2 Ermm Cd3d Cd3e Cd3g Cd4 Cd8a Thy1 Ptprcap Ltb Stab1 Pf4 Ms4a7 Mrc1 F13a1 Dab2 Col3a1 Col5a2 Cxcl2 Lgals3
Average Expression
2
1
0
-1
Percent Expressed
0
25
50
75
100
b
All
CON
EA
Oligodendrocytes
Fibroblasts
Endothelial cells
T cells
BAMs
Granulocyte
Microglia
Astrocytes
tSNE_1
tSNE_2
Endothelial cells
Astrocytes
Microglia
Oligodendrocytes
T cells
BAMs
Fibroblasts
Granulocyte
c
Astrocytes
Aldoc Pla2g7 Ptprz1 Ndrg2 Acsl12 Acsl6 Agt Aqp4 Atp1b2 Bcan Cldn10 Dclk1 Atp1a2 Gja1 Ntsr2
Endothelial cells
Rgs5 Abcg2 Acvrl1 Car4 Cdh5 Cldn5 Clic5 Itm2a
Microglia
Rhob Gpr34 Cst3 Hexb C1qa C1qb C1qc Ctss Itgam Ccr5 Aif1 Cd68 Tgfbr1 Tgfbr2 Sparc Olfml3 Lrp1 Cd81
Granulocytes
Cxcl2
Lgals3
Oligodendrocytes
Sox10 Mbp Plp1 Apod Aspa Ccp110 Cldn11 Cntn2 Efnb3 Enpp2 Ermn
T cells
Cd3d Cd3e Cd3g Cd4 Cd8a Thy1 Ptprcap Ltb
BAMs
Stab1 Pf4 Ms4a7 Mrc1 F13a1 Dab2
Fibroblasts
Col3a1 Col5a2
Expression Level
Identity

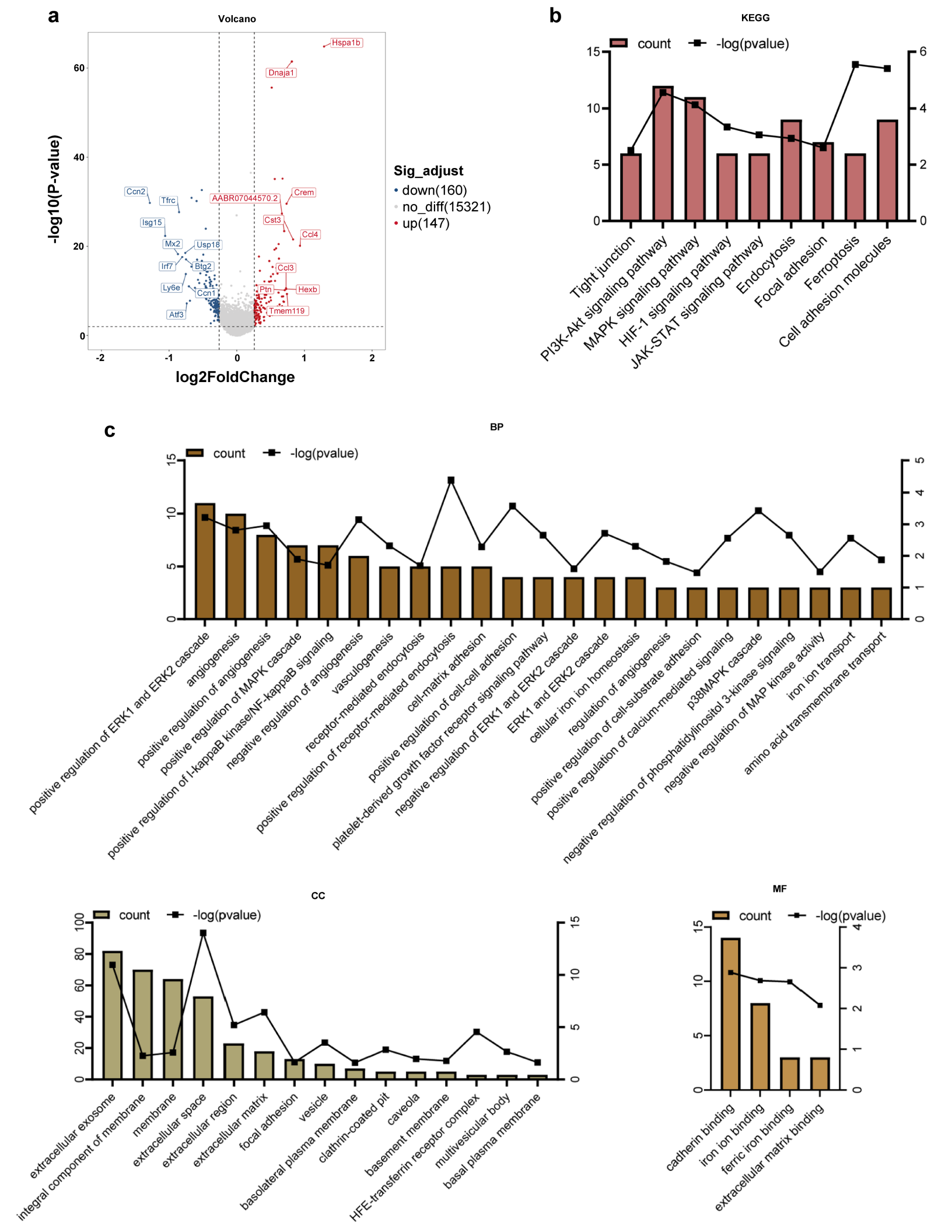
a
Volcano
-log10(P-value)
log2FoldChange
Hspa1b
Dnaja1
Crem
AABR07044570.2
Cst3
Ccl4
Ccl3
Hexb
Ptn
Tmem119
Ccn2
Tfrc
Isg15
Mx2
Usp18
Irf7
Btg2
Ly6e
Ccn1
Atf3
Sig_adjust
down(160)
no_diff(15321)
up(147)
b
KEGG
count
-log(pvalue)
Tight junction
PI3K-Akt signaling pathway
MAPK signaling pathway
HIF-1 signaling pathway
JAK-STAT signaling pathway
Endocytosis
Focal adhesion
Ferroptosis
Cell adhesion molecules
c
BP
count
-log(pvalue)
positive regulation of ERK1 and ERK2 cascade
angiogenesis
positive regulation of angiogenesis
positive regulation of MAPK cascade
positive regulation of I-kappaB kinase/NF-kappaB signaling
negative regulation of angiogenesis
vasculogenesis
receptor-mediated endocytosis
positive regulation of receptor-mediated endocytosis
cell-matrix adhesion
positive regulation of cell-cell adhesion
platelet-derived growth factor receptor signaling pathway
negative regulation of ERK1 and ERK2 cascade
ERK1 and ERK2 cascade
cellular iron ion homeostasis
regulation of angiogenesis
positive regulation of cell-substrate adhesion
positive regulation of calcium-mediated signaling
p38MAPK cascade
negative regulation of phosphatidylinositol 3-kinase signaling
negative regulation of MAP kinase activity
iron ion transport
amino acid transmembrane transport
CC
count
-log(pvalue)
extracellular exosome
integral component of membrane
membrane
extracellular space
extracellular region
extracellular matrix
focal adhesion
vesicle
basolateral plasma membrane
clathrin-coated pit
caveola
basement membrane
HFE-transferrin receptor complex
multivesicular body
basal plasma membrane
MF
count
-log(pvalue)
cadherin binding
iron ion binding
ferric iron binding
extracellular matrix binding

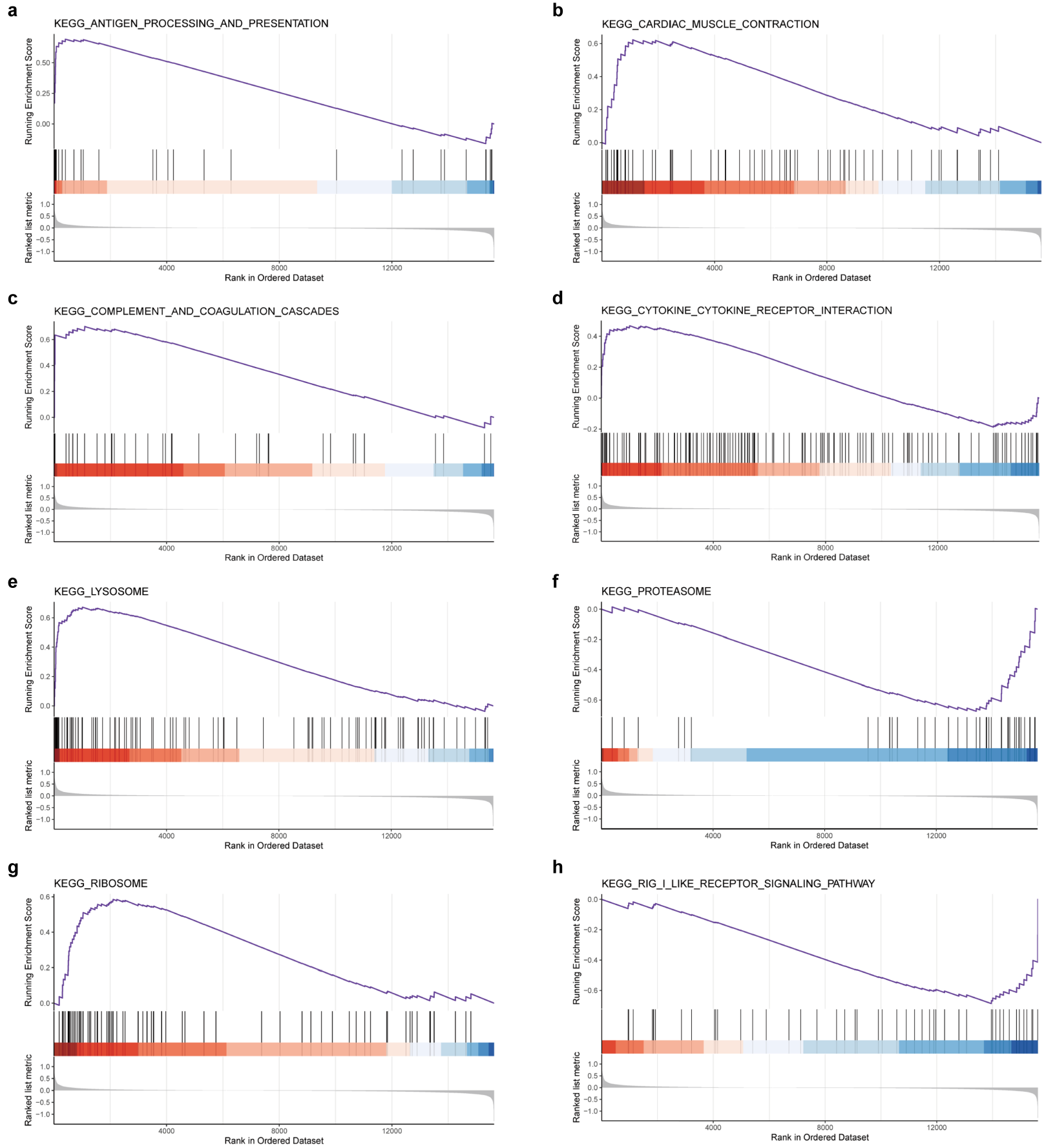
a
KEGG_ANTIGEN_PROCESSING_AND_PRESENTATION
b
KEGG_CARDIAC_MUSCLE_CONTRACTION
c
KEGG_COMPLEMENT_AND_COAGULATION_CASCADES
d
KEGG_CYTOKINE_CYTOKINE_RECEPTOR_INTERACTION
e
KEGG_LYSOSOME
f
KEGG_PROTEASOME
g
KEGG_RIBOSOME
h
KEGG_RIG_I_LIKE_RECEPTOR_SIGNALING_PATHWAY
Running Enrichment Score
Ranked list metric
Rank in Ordered Dataset
4000
8000
12000

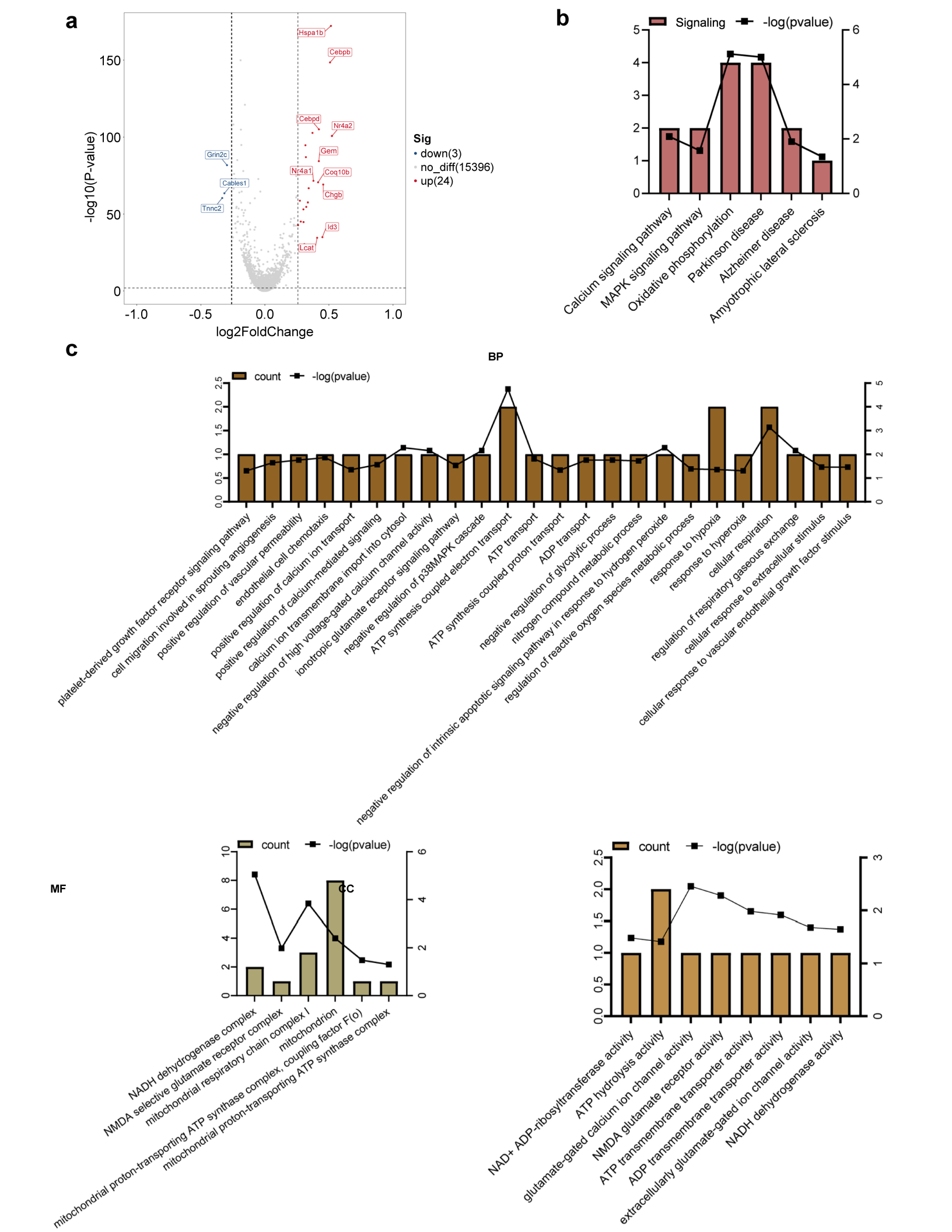
a
-log10(P-value)
log2FoldChange
Hspa1b
Cebpb
Cebpd
Nr4a2
Gem
Nr4a1
Coq10b
Chgb
Id3
Lcat
Grin2c
Cables1
Tnnc2
Sig
down(3)
no_diff(15396)
up(24)
b
Signaling
-log(pvalue)
Calcium signaling pathway
MAPK signaling pathway
Oxidative phosphorylation
Parkinson disease
Alzheimer disease
Amyotrophic lateral sclerosis
c
BP
count
-log(pvalue)
platelet-derived growth factor receptor signaling pathway
cell migration involved in sprouting angiogenesis
positive regulation of vascular permeability
endothelial cell chemotaxis
positive regulation of calcium ion transport
positive regulation of calcium-mediated signaling
calcium ion transmembrane import into cytosol
negative regulation of high voltage-gated calcium channel activity
ionotropic glutamate receptor signaling pathway
negative regulation of p38MAPK cascade
ATP synthesis coupled electron transport
ATP transport
ATP synthesis coupled proton transport
ADP transport
negative regulation of glycolytic process
nitrogen compound metabolic process
negative regulation of intrinsic apoptotic signaling pathway in response to hydrogen peroxide
regulation of reactive oxygen species metabolic process
response to hypoxia
response to hyperoxia
cellular respiration
regulation of respiratory gaseous exchange
cellular response to extracellular stimulus
cellular response to vascular endothelial growth factor stimulus
MF
count
-log(pvalue)
NADH dehydrogenase complex
NMDA selective glutamate receptor complex
mitochondrial respiratory chain complex I
mitochondrion
mitochondrial proton-transporting ATP synthase complex, coupling factor F(o)
mitochondrial proton-transporting ATP synthase complex
CC
count
-log(pvalue)
NAD+ ADP-ribosyltransferase activity
ATP hydrolysis activity
glutamate-gated calcium ion channel activity
NMDA glutamate receptor activity
ATP transmembrane transporter activity
ADP transmembrane transporter activity
extracellularly glutamate-gated ion channel activity
NADH dehydrogenase activity

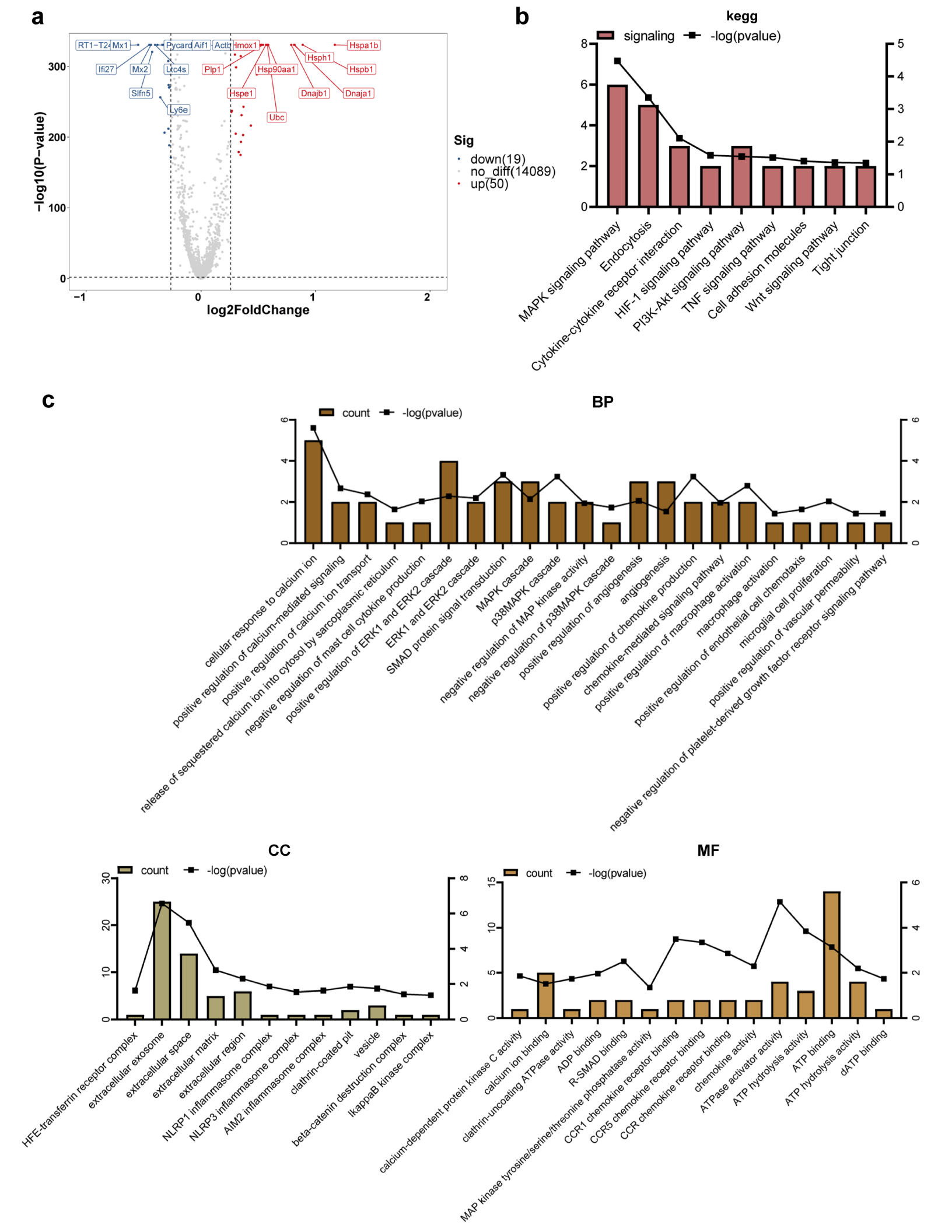
a
RT1−T24
Mx1
Pycard
Aif1
Actb
Hmox1
Hspa1b
Hsph1
Hspb1
Ifi27
Mx2
Ltc4s
Plp1
Hsp90aa1
Slfn5
Hspe1
Dnajb1
Dnaja1
Ly6e
Ubc
−log10(P−value)
log2FoldChange
Sig
down(19)
no_diff(14089)
up(50)
b
kegg
signaling
-log(pvalue)
MAPK signaling pathway
Endocytosis
Cytokine-cytokine receptor interaction
HIF-1 signaling pathway
PI3K-Akt signaling pathway
TNF signaling pathway
Cell adhesion molecules
Wnt signaling pathway
Tight junction
c
BP
count
-log(pvalue)
cellular response to calcium ion
positive regulation of calcium-mediated signaling
positive regulation of calcium ion transport
positive regulation of calcium ion into cytosol by sarcoplasmic reticulum
release of sequestered calcium ion into cytosol by sarcoplasmic reticulum
negative regulation of mast cell cytokine production
positive regulation of ERK1 and ERK2 cascade
ERK1 and ERK2 cascade
SMAD protein signal transduction
MAPK cascade
p38MAPK cascade
negative regulation of MAP kinase activity
negative regulation of p38MAPK cascade
positive regulation of angiogenesis
angiogenesis
positive regulation of chemokine production
chemokine-mediated signaling pathway
positive regulation of macrophage activation
macrophage activation
positive regulation of endothelial cell chemotaxis
microglial cell proliferation
positive regulation of vascular permeability
negative regulation of platelet-derived growth factor receptor signaling pathway
CC
count
-log(pvalue)
HFE-transferrin receptor complex
extracellular exosome
extracellular space
extracellular matrix
extracellular region
NLRP1 inflammasome complex
NLRP3 inflammasome complex
AIM2 inflammasome complex
clathrin-coated pit
vesicle
beta-catenin destruction complex
IkappaB kinase complex
MF
count
-log(pvalue)
calcium-dependent protein kinase C activity
calcium ion binding
clathrin-uncoating ATPase activity
ADP binding
R-SMAD binding
MAP kinase tyrosine/serine/threonine phosphatase activity
CCR1 chemokine receptor binding
CCR5 chemokine receptor binding
CCR chemokine receptor binding
chemokine activity
ATPase activator activity
ATP hydrolysis activity
ATP binding
ATP hydrolysis activity
dATP binding

a
orig.ident
CON
EA
UMAP_1
UMAP_2
tSNE_1
tSNE_2
b
EC_Cluster 0
EC_Cluster 2
EC_Cluster 4
EC_Cluster 5
Percent Expressed
Average Expression
Identity
Features
c
EC_Cluster0_GO BarPlot
EC_Cluster0_KEGG BarPlot
EC_Cluster0_KEGG ScatterPlot
Biological Process
Cellular Component
Molecular Function
Gene Number
GO Term
Pathway Name
Cellular Processes
Environmental Information Processing
Genetic Information Processing
Human Diseases
Organismal Systems
Pathway
Rich Factor
P.value
d
EC_Cluster2_GO BarPlot
EC_Cluster2_KEGG BarPlot
EC_Cluster2_KEGG ScatterPlot
e
EC_Cluster4_GO BarPlot
EC_Cluster4_KEGG BarPlot
EC_Cluster4_KEGG ScatterPlot
f
EC_Cluster5_GO BarPlot
EC_Cluster5_KEGG BarPlot
EC_Cluster5_KEGG ScatterPlot